ISSN 1674-1056
http://cpb.iphy.ac.cn
http://iopscience.iop.org/cpb
中国物理 B
Chinese Physics
中国物理 Chinese Physics B

Observation of large in-plane anisotropic transport in van der Waals semiconductor Nb_2SiTe_4

Kaiyao Zhou(周楷尧), Jun Deng(邓俊), Long Chen(陈龙), Wei Xia(夏威), Yanfeng Guo(郭艳峰), Yang Yang(杨洋), Jian-Gang Guo(郭建刚), and Liwei Guo(郭丽伟)

Citation: Chin. Phys. B, 2021, 30 (**8**): 087202. DOI: 10.1088/1674-1056/ac068f
Journal homepage: http://cpb.iphy.ac.cn; http://iopscience.iop.org/cpb

What follows is a list of articles you may be interested in

Group velocity matters for accurate prediction of phonon-limited carrier mobility

Qiao-Lin Yang(杨巧林), Hui-Xiong Deng(邓惠雄), Su-Huai Wei(魏苏淮), and Jun-Wei Luo(骆军委)
Chin. Phys. B, 2021, 30 (**8**): 087201. DOI: 10.1088/1674-1056/ac0133

Effect of Nb doping on microstructures and thermoelectric properties of $SrTiO_3$ ceramics

Da-Quan Liu(刘达权), Yu-Wei Zhang(张玉伟), Hui-Jun Kang(康慧君), Jin-Ling Li(李金玲), Xiong Yang(杨雄), Tong-Min Wang(王同敏)
Chin. Phys. B, 2018, 27 (**4**): 047205. DOI: 10.1088/1674-1056/27/4/047205

First-principles hybrid functional study of the electronic structure and charge carrier mobility in perovskite $CH_3NH_3SnI_3$

Li-Juan Wu(伍丽娟), Yu-Qing Zhao(赵宇清), Chang-Wen Chen(陈畅文), Ling-Zhi Wang(王琳芝), Biao Liu(刘标), Meng-Qiu Cai(蔡孟秋)
Chin. Phys. B, 2016, 25 (**10**): 107202. DOI: 10.1088/1674-1056/25/10/107202

High temperature characteristics of bilayer epitaxial graphene field-effect transistors on SiC Substrate

Ze-Zhao He(何泽召), Ke-Wu Yang(杨克武), Cui Yu(蔚翠), Qing-Bin Liu(刘庆彬), Jing-Jing Wang(王晶晶), Jia Li(李佳), Wei-Li Lu(芦伟立), Zhi-Hong Feng(冯志红), Shu-Jun Cai(蔡树军)
Chin. Phys. B, 2016, 25 (**6**): 067206. DOI: 10.1088/1674-1056/25/6/067206

Radio-frequency transistors from millimeter-scale graphene domains

Wei Zi-Jun, Fu Yun-Yi, Liu Jing-Bo, Wang Zi-Dong, Jia Yue-Hui, Guo Jian, Ren Li-Ming, Chen Yuan-Fu, Zhang Han, Huang Ru, Zhang Xing
Chin. Phys. B, 2014, 23 (**11**): 117201. DOI: 10.1088/1674-1056/23/11/117201

Observation of large in-plane anisotropic transport in van der Waals semiconductor Nb_2SiTe_4*

Kaiyao Zhou(周楷尧)[1,2], Jun Deng(邓俊)[1,2], Long Chen(陈龙)[1,2], Wei Xia(夏威)[4,5], Yanfeng Guo(郭艳峰)[4,5], Yang Yang(杨洋)[1,2], Jian-Gang Guo(郭建刚)[1,3,†], and Liwei Guo(郭丽伟)[1,2,3,‡]

[1] *Beijing National Laboratory for Condensed Matter Physics, Institute of Physics, Chinese Academy of Sciences, Beijing* 100190, *China*
[2] *University of Chinese Academy of Sciences, Beijing* 100049, *China*
[3] *Songshan Lake Materials Laboratory, Dongguan* 523808, *China*
[4] *School of Physical Science and Technology, ShanghaiTech University, Shanghai* 201210, *China*
[5] *ShanghaiTech Laboratory for Topological Physics, ShanghaiTech University, Shanghai* 201210, *China*

(Received 9 April 2021; revised manuscript received 8 May 2021; accepted manuscript online 29 May 2021)

Two-dimensional (2D) van der Waals material is a focus of research for its widespread application in optoelectronics, memories, and spintronics. The ternary compound Nb_2SiTe_4 is a van der Waals semiconductor with excellent air stability and small cleavage energy, which is suitable for preparing a few layers counterpart to explore novel properties. Here, properties of bulk Nb_2SiTe_4 with large in-plane electrical anisotropy are demonstrated. It is found that hole carriers dominate at a temperature above 45 K with a carrier active energy of 31.3 meV. The carrier mobility measured at 100 K is about 213 $cm^2 \cdot V^{-1} \cdot s^{-1}$ in bulk Nb_2SiTe_4, higher than the reported results. In a thin flake Nb_2SiTe_4, the resistivity ratio between the crystalline axes of *a* and *b* is reaching about 47.3 at 2.5 K, indicating that there exists a large anisotropic transport behavior in their basal plane. These novel transport properties provide accurate information for modulating or utilizing Nb_2SiTe_4 for electronic device applications.

Keywords: carrier mobility, anisotropic transport, Raman spectroscopy

PACS: 72.80.Ga,72.20.Fr, 74.25.nd **DOI:** 10.1088/1674-1056/ac068f

1. Introduction

Two-dimensional (2D) van der Waals materials have triggered great interests in recent decades for the fact that a few atomic layers samples can be easily exfoliated from the bulk materials, which own various thickness-dependent physical properties[1–4] and are constitutional units for 2D heterojunction devices.[5–7] They have a widespread application in optoelectronics, memories, and so on.[8,9] In the past decades, graphene has been widely studied due to its high carrier mobility and other peculiar properties,[10–15] but the gapless band structure strongly limits its usability for conventional logical transistors.[16] Thereafter, searching 2D semiconductors with tunable bandgap is highly desired. Layered transition metal dichalcogenide (TMDC), such as MX_2 (M = Zr, Hf, Mo, W; X = S, Se), is the representative compound of the 2D van der Waals semiconductors with a bandgap about 0.2–1.6 eV[17] and carrier mobility from 30 $cm^2 \cdot V^{-1} \cdot s^{-1}$ to 480 $cm^2 \cdot V^{-1} \cdot s^{-1}$ depending on the supporting substrates and gate voltages.[18–20] Besides TMDC, the latest researches on ternary alloys with van der Waals layered structures have become the new focuses, such as $MnBi_2Te_4$,[3] which is the first discovered intrinsic magnetic topological insulator, exhibiting quantized anomalous Hall effect in its film.[21–23]

Similarly, studies on Nb_2SiTe_4, a 2D van der Waals semiconductor, have been reignited recently,[24] although the bulk material was firstly reported in 1993.[25] It has been reported that Nb_2SiTe_4 is a highly stable, narrow bandgap (0.39 eV) and ferroelastic layered semiconductor[26] with high carrier mobility (about 100 $cm^2 \cdot V^{-1} \cdot s^{-1}$ at 100 K). Thus, few-layer Nb_2SiTe_4 was prepared by mechanical exfoliation to study its properties, which was stable under ambient conditions.[24] The ambipolar carrier transport was observed in Nb_2SiTe_4 with a gate modulation.[24] Besides, Zhang *et al.* found that monolayer Nb_2SiTe_4 processes reversible ferroelastic under strain.[26] Furthermore, theoretical calculations predicted that the electron (hole) carrier mobilities of *a*-direction and *b*-direction are 1775(114) $cm^2 \cdot V^{-1} \cdot s^{-1}$ and 1222(73) $cm^2 \cdot V^{-1} \cdot s^{-1}$ from the Bardeen–Shockley formula,[27,28] respectively. All of these indicate that Nb_2SiTe_4 is a potential 2D layered semiconductor with high carrier mobility and ambipolar carrier transport. However, up to now, there is no report concerning experimental results of carrier transport along the crystalline axes in the basal plane, which is important in constituting 2D devices.

*Project supported by the National Key Research and Development Program of China (Grant Nos. 2018YFE0202600, 2016YFA0300600, and 2017YFA0304700), by the National Natural Science Foundation of China (Grant Nos. 51922105, 51772322, and 11704401), and Beijing Natural Science Foundation (Grant No. Z200005).

†Corresponding author. E-mail: jgguo@iphy.ac.cn
‡Corresponding author. E-mail: lwguo@iphy.ac.cn

© 2021 Chinese Physical Society and IOP Publishing Ltd

Furthermore, it is not clear that the ambipolar carriers exist simultaneously or separately in the material, both of which are important for exploring Nb_2SiTe_4 based 2D layered devices and their 2D heterojunction devices.

In this work, studies on carrier transport properties of semiconductor Nb_2SiTe_4 are reported. It is found that hole carriers dominate in a thick flake of Nb_2SiTe_4 above 45 K. The hole carrier active energy is deduced to be about 31.3 meV by fitting the temperature-dependent carrier concentration curve. Meanwhile, a large carrier transport anisotropy is found. That is, the ratio between resistivities along the crystalline axes of *a* and *b* measured on Nb_2SiTe_4 thin flake is about 47.3 at 2.5 K. These special features in Nb_2SiTe_4 are extremely important for constructing 2D devices. The detailed analysis and discussion on these experimental results are presented below.

2. Experimental methods

2.1. Growth of Nb_2SiTe_4 single crystals

Single crystal of layered Nb_2SiTe_4 was grown by solid reaction method using Si and Te as a flux. All the raw materials of Nb, Si, and Te are powder with purity 99.99%, which were mixed uniformly in an atomic ratio of Nb:Si:Te = 1:2:8. Then they were loaded into an Al_2O_3 crucible in the argon-filled gloved box with low moisture and oxygen levels (< 0.1 ppm). The crucible was placed in a quartz tube and the tube was flame-sealed under a high vacuum. Next, the sealed quartz tube was placed in a well furnace and heated to 1420 K in 10 h and kept for 5 h. Then the furnace was slowly cooled down to 1020 K at a rate of 1 K/h. The flux was then removed with a centrifuge process. When the ampoule was fully cooled down to room temperature, it was broken to take the synthesized single crystals out. A thin flake Nb_2SiTe_4 was easily obtained through the mechanical exfoliation method, and the detailed exfoliation process was described in the literature.[29]

2.2. Characterization and electrical measurements

Powder x-ray diffraction (XRD) pattern of the prepared Nb_2SiTe_4 samples was measured by a PANalytical X'Pert PRO diffractometer with a Cu $K\alpha$ ($\lambda = 1.5408$ Å) radiation. The chemical composition and microtopography of the samples were analyzed by a scanning electron microscope (SEM) equipped with energy dispersive spectrum (EDS). The crystalline directions in the basal plane of a thin flake were determined by an angle-resolved polarized Raman spectroscopy (ARPRS) to facilitate the measurement of crystalline orientation-dependent carrier transport properties. The polarized Raman spectra were probed by a HORIBA LabRAM HR Evolution Raman spectrometer with a 532 nm laser in back scattering geometry. The incident light was linearly polarized, and a polarizer was used to change the polarization direction of the scattered light. When the polarization directions of the incident light and scattered light are parallel, it is called the parallel polarized configuration, while they are perpendicular, it is called the cross polarized configuration. The thickness of a thin flake sample was determined by atomic force microscopy (AFM) (Bruker AFM Multimode 8). The carrier transport properties were measured in a physical property measurement system (PPMS, Quantum Design). A standard Hall bar pattern with Ti/Au electrodes was adopted for Hall measurement on thick Nb_2SiTe_4 single crystal samples. And a standard four-terminal resistance measurement was used in a thin flake of Nb_2SiTe_4 for crystalline orientation-dependent transport property study. Here two groups of the electrodes on the same sample are respectively along the crystalline axes of *a* and *b*. The electrodes in thickness of 10 nm (Ti)/90 nm (Au) were deposited by electronic beam deposition (EBD). Here, the electrode pattern was transferred from a homemade Mo-mask onto the top of a thick Nb_2SiTe_4 sample. While the electrode pattern on a thin flake of Nb_2SiTe_4 was prepared with the help of electron beam lithography (EBL). Metal Ti is selected as an electrode material because its electron work function of 4.33 eV is close to that of Nb_2SiTe_4 about 4.36 eV.[24] This ensures a good ohmic contact between Ti and the Nb_2SiTe_4 sample,[24] supported by a perfect linear relationship of the raw *I*–*V* curve, as shown in Fig. S1.

2.3. Phonon vibration mode calculations of Nb_2SiTe_4 single crystal

The phonon vibration modes of Nb_2SiTe_4 single crystal were calculated with the computational procedure of QUANTUMN-ESSPRESSO code[30] within the framework of linear response theory. We employed the optimized norm-conserving Vanderbilt (ONCV) pseudopotential[31] with local density approximation (LDA) for exchange–correlation potentials. The plane wave cutoff energy was set as 80 Ry and the Monkhorst–Pack mesh of points $8 \times 6 \times 4$ was used in the Brillouin zone integration. Atomic positions and lattice parameters were relaxed until all the forces on the ions were less than 10^{-5} Ry/Bohr and the total energy changed less than 10^{-5} Ry between two adjacent ionic steps.

3. Results and discussion

The obtained Nb_2SiTe_4 single crystals with metallic luster and the average size of 2–4 mm in width and 10–200 μm in thickness are shown in the inset of Fig. 1(a). From the results of EDS as shown in Fig. S2 and Table S2 of supporting material, the atomic ratio of Nb:Si:Te is close to the nominal stoichiometry. The XRD pattern of a Nb_2SiTe_4 single crystal sample is shown in Fig. 1(a), which only consists of the (00*l*) diffraction peaks, suggesting that it is a [001] orientated single crystal with a layer spacing 7.03 Å (or crystal parameters

a, b, and c equal to 6.3 Å, 7.9 Å, and 14.72 Å in monoclinic lattice), which is close to the reported value.[24] The lamellar shape of the as-grown Nb_2SiTe_4 crystals suggests that it is a typical layered structure. Its crystal structure is schematically drawn in Figs. 1(b) and 1(c) with side and top views, respectively. While viewing along b-direction, Nb and Si are respectively bonded with Te atoms and are sandwiched in the middle of two Te atomic layers. Each crystalline unit cell contains two such layers stacked along the c-direction.

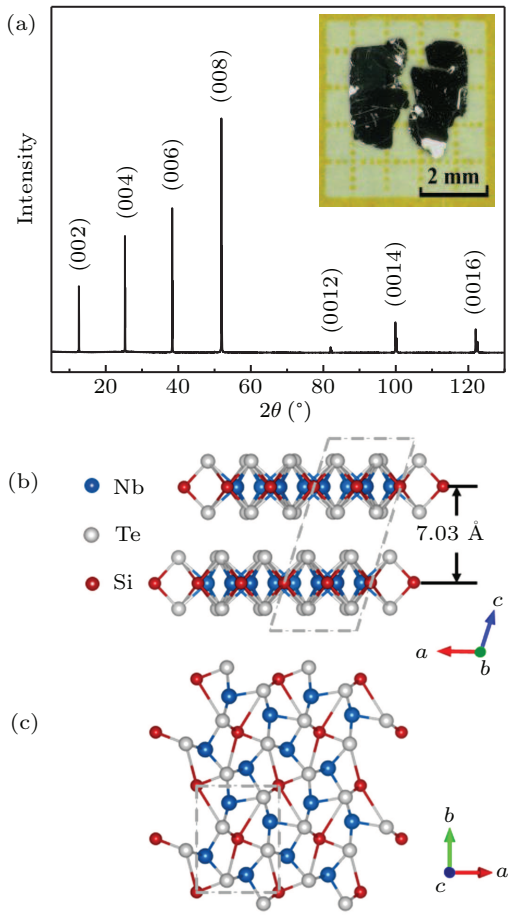


Fig. 1. XRD pattern of Nb_2SiTe_4 and its crystal structure. (a) XRD pattern of Nb_2SiTe_4 single crystal. Inset is an optical photo of an as-grown Nb_2SiTe_4 single crystal. (b) Side view of Nb_2SiTe_4 crystal structure along the b-direction. The unit cell is schematically shown as the dashed gray line, where Nb, Si, and Te atoms are shown as blue, gray, and red spheres, respectively. The interlayer distance is 7.03 Å determined by the XRD data. (c) Top view of Nb_2SiTe_4 crystal structure.

The temperature-dependent transport properties were measured from 1.5 K to 300 K as shown in Fig. 2. Figure 2(a) shows the temperature dependence of electrical resistivity ρ_{xx} of samples 1 and 2 without magnetic field. The thicknesses of samples 1 and 2 are 40 μm and 130 μm, respectively. It is noted that their electrical transport behaviors are similar, but their absolute values are different, which may be ascribed to large anisotropic transport behavior in the basal plane as analyzed below. The resistivity rapidly decreases with temperature increasing, suggesting semiconducting behavior over the full temperature range. Furthermore, the carrier concentration and mobility of samples 1 and 2 were also studied through the Hall measurement. Here the results from sample 1 are shown in Figs. 2(b)–2(d) and those from sample 2 are shown in Fig. S3. In Fig. 2(b), it is found that the slopes of the Hall resistivity ρ_{xy} are positive and monotonically increased with temperature decreasing at the temperature above 55 K, which indicates the majority of carriers are holes. Below 55 K, the slope of Hall resistivity shows decreasing and even changing sign from obvious positive to weakly negative below 10 K, hinting the electrons contribution might appear. This speculation needs further experimental studies in the future. In the following, quantitative analyses on the carrier concentration and mobilities are based on the experimental data above 55 K. The carrier concentration and mobility are deduced from $n = \mathrm{d}B/\mathrm{d}\rho_{xy}/e$ and $\mu = 1/(ne\rho_{xx})$, where e denotes the elementary charge and B the applied magnetic field. Figure 2(c) depicts the temperature dependence of carrier concentration n and carrier mobility μ labeled with hollow circle and triangle symbols, respectively. It is seen that the hole carrier concentration shows a monotonous decrease from 300 K to 55 K. This carrier concentration variation with temperature is fitted based on a single energy level model, $n(T) = N_\mathrm{h}\exp(-E_\mathrm{h}/k_\mathrm{B}T)$, where N_h, E_h, and k_B are the acceptor density, hole activation energy, and Boltzmann constant, respectively. It is deduced that the hole activation energy E_h is about 31.3 meV and the acceptor density is about 6.13×10^{17} cm^{-3}. The phenomena observed in Fig. 2(b) suggest that the activated donors at low temperature should have smaller active energy and density compared with that of acceptors, so that net hole carriers are observed at temperature above 55 K. It is speculated that the intrinsic defects in Te atoms might be responsible for the carrier doping because there is around 10% Te deficiency as seen in Table S2 of supporting material. Besides, the carrier mobility first increases from 300 K to 100 K and then decreases with cooling. The maximal value in carrier mobility is 213 $\mathrm{cm}^2\cdot\mathrm{V}^{-1}\cdot\mathrm{s}^{-1}$ at 100 K, similar to that of sample 2 as shown in Fig. S3 of supporting material. The carrier mobility value is far higher than the theoretical prediction[27] and the reported experimental results.[24]

To study the electrical anisotropy of Nb_2SiTe_4, a thin flake Nb_2SiTe_4 was exfoliated, whose thickness is 16.8 nm measured by AFM as shown in Fig. S4, to study dependence of its Raman signal intensity on crystalline directions and to identify the crystalline axes. Its crystalline axis directions in the basal plane were determined by the ARPRS, because its Raman signal intensity is strongly dependent on the crystalline orientations.[32] The space group of Nb_2SiTe_4 is $P2_1/c$ (No. 14) and the corresponding point group is $C_{2h}(2/m)$, whose Raman activity modes are $21\mathrm{A_g} + 21\mathrm{B_g}$.[33] Figure 3 shows the polarized Raman spectrum of the 16.8 nm thin flake under the parallel polarized

configuration.[34] The incident light is polarized in $\boldsymbol{e}_{\rm i}$ direction, $\boldsymbol{e}_{\rm i} = (\cos(\theta+\varphi), \sin(\theta+\varphi), 0)$, where θ is the angle between the incident light polarization direction and user-defined x-axis [see Fig. 3(a)] and φ is the angle between the x-axis and a-direction. Figure 3(b) shows the measured Raman spectrum under a parallel polarized configuration. Based on the Raman tensor of space group $P2_1/c$, the density functional theory (DFT) calculation gives all the Raman active modes, whose Raman peak positions are shown in Fig. 3(b) marked with the short bars. It is noted that five relatively strong Raman modes are observed in the Raman spectrum, which are corresponding to the Raman shifts at 94.79 cm^{-1}, 121.41 cm^{-1}, 133.91 cm^{-1}, 160.90 cm^{-1}, and 204.78 cm^{-1}, respectively. These Raman peaks show two- or four-fold symmetry when the sample is rotated in the measurement processes shown in Fig. S5.1 of supporting material. For example, the angular dependence of the A_g modes located at 121.41 cm^{-1} and 160.90 cm^{-1} in parallel polarized configuration exhibits two-fold symmetry, see Figs. 4(a) and 4(b), respectively. The other typical Raman modes located at 94.79 cm^{-1} and 204.78 cm^{-1} are also clearly observed on ARPRS as shown in Fig. S5.2. Besides, the similar two-dimensional contour plots of angular dependence Raman spectra collected from the same sample in a cross polarized configuration were also measured and shown in Fig. S5.3 of supporting material.

Here we choose the typical modes for quantitative analysis. The intensity of the Raman signal is expressed as

$$I \propto |\boldsymbol{e}_{\rm i} \cdot \boldsymbol{R} \cdot \boldsymbol{e}_{\rm s}|^2,$$

where $\boldsymbol{e}_{\rm s}$ is the unit polarization vector of the scattered light and $\boldsymbol{R}$ the Raman tensor. For space group $P2_1/c$, the Raman tensors for A_g and B_g modes are[33]

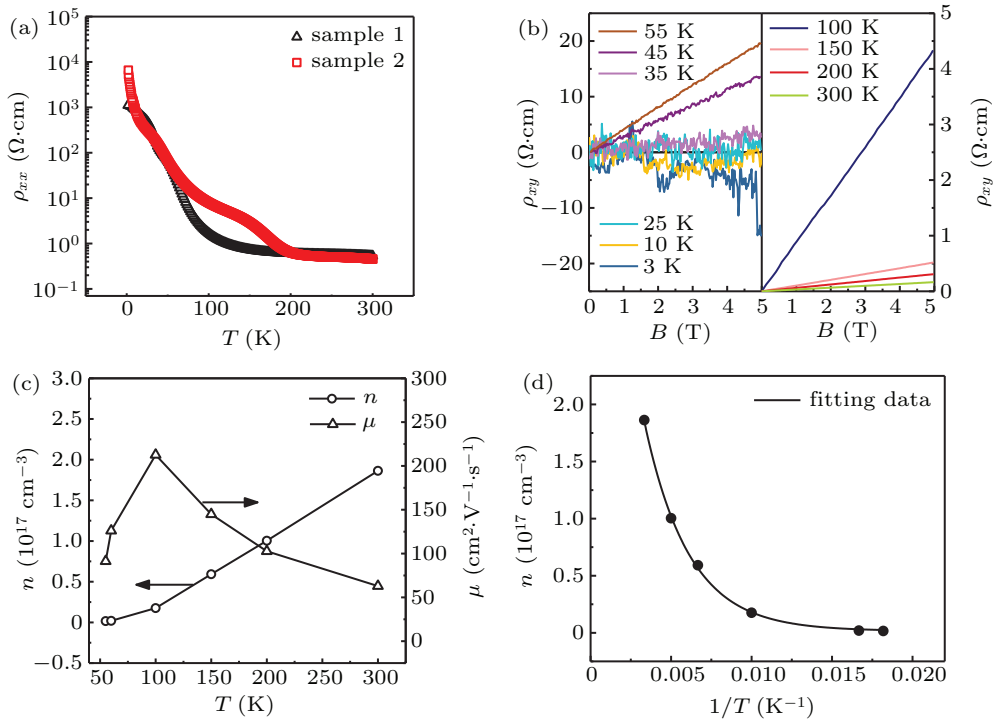


Fig. 2. Temperature dependence of transport properties. (a) Bulk longitudinal resistivity ρ_{xx} under 0 T. (b) Hall resistivity ρ_{xy}. (c) Carrier concentration n and mobility μ. (d) A fitting to carrier density as a function of reciprocal temperature.

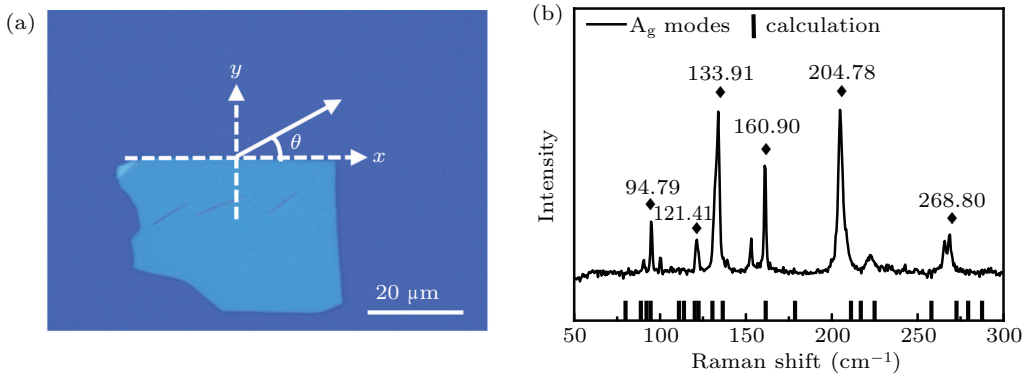


Fig. 3. Polarized Raman spectrum from a thin flake of Nb_2SiTe_4. (a) Optical image of a thin flake Nb_2SiTe_4 device with schematic coordinate system and the rotation angle definition. (b) Polarized Raman spectrum with a parallel polarized configuration. The short bars are the calculated Raman peak positions.

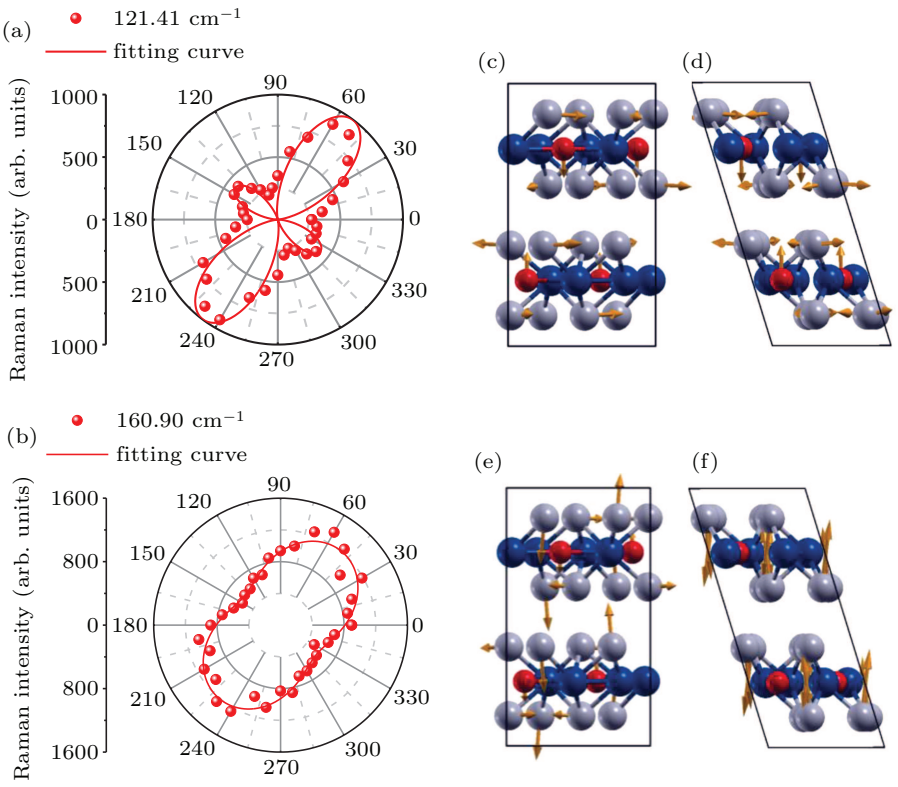


Fig. 4. Two typical Raman modes in the parallel polarized configuration. (a) and (b) Polar diagrams of the peak intensities for the A_g modes at 121.41 cm^{-1} and 160.90 cm^{-1}, respectively. (c) and (d) Schematic diagrams of A_g mode at 121.41 cm^{-1} in front and side views, respectively. (e) and (f) Schematic diagrams of A_g mode at 160.90 cm^{-1} in front and side views, respectively.

$$R_{A_g} = \begin{pmatrix} a & d & 0 \\ d & b & 0 \\ 0 & 0 & c \end{pmatrix}, \quad R_{B_g} = \begin{pmatrix} 0 & 0 & e \\ 0 & 0 & f \\ e & f & 0 \end{pmatrix},$$

where a, b, c, d, e, and f are the Raman tensor elements. In the parallel polarized configuration, the $\boldsymbol{e}_s = (\cos(\theta+\varphi), \sin(\theta+\varphi), 0)$, where θ and ϕ are defined above. The intensities of the A_g and B_g modes are given as

$$I^{\parallel}_{A_g} \propto \left[a\cos^2(\theta+\varphi) + b\sin^2(\theta+\varphi) + d\sin^2(\theta+\varphi)\right]^2,$$
$$I^{\parallel}_{B_g} = 0.$$

From the second equation above, we can find that all the B_g modes would not be observed in polarized Raman spectrum with parallel polarized configuration. Therefore, the A_g modes were observed. Figures 4(a) and 4(b) plot the angular dependence of A_g phonon modes at 121.41 cm^{-1} and 160.90 cm^{-1}, while the other A_g modes are shown in Fig. S5.3 of supporting material. We can fit the data in Figs. 4(a) and 4(b) using $I^{\parallel}_{A_g} = K\left[a\cos^2(\theta+\varphi) + b\sin^2(\theta+\varphi) + d\sin^2(\theta+\varphi)\right]^2$, and identify the largest intensity which is in close to 50° relative to the x-axis. The atomic vibration modes for the A_g modes of 121.41 cm^{-1} and 160.90 cm^{-1} are schematically shown in Figs. 4(c)–4(f) in front and side views. A similar analysis of Raman peak intensities in the cross polarized configuration is shown in Fig. S5.3 of supporting material. For the A_g mode of 160.90 cm^{-1}, the atomic displacement has components in a- and c-direction, indicating the largest intensity component in the basal plane is along the a-direction.

Based on the results from ARPRS and experience of identifying crystalline axes in the basal plane, a fresh thin flake Nb_2SiTe_4 sample was prepared and its crystalline axes in the basal plane were identified by recording intensities distribution of the Raman peak located at 160.90 cm^{-1} as given in Fig. S5.4(a) of supporting material. It was determined that the a-direction is proximity to −10° off the defined x-axis, and the b-direction is rotated to −100° relative to the x-axis, as marked in Fig. 5(a). Here, the counterclockwise direction is defined as the positive direction. According to the known directions, two groups of four-terminal electrodes along its crystalline axes of a and b were fabricated on the thin flake Nb_2SiTe_4 sample as shown in Fig. 5(a), using a standard device procedure as stated in Section 2. The four-terminal resistance measurement is a reliable method to eliminate the effect of contact resistance on transport properties, especially on studying anisotropic transport properties. The resistivities along the a- and b-direction were measured from 2.5 K to 300 K as shown in Fig. 5(b). It is found that the resistivity variation with temperature is similar to that observed in the thick Nb_2SiTe_4 sample as shown in Fig. 2(a). However, the resistivity measured along the a-direction is larger than that along the b-direction over the whole test temperature range. In detail, the variation of the ratio ρ^a_{xx}/ρ^b_{xx} with the temperature is given in Fig. 5(c). It is found that the ratio is steeply decreasing from about 47.3 to 5 with temperature increasing from 2.5 K to about 25 K,

then gradually decreases from 5 to 1.7 at 300 K as shown in Fig. 5(c). Such large transport anisotropy is consistent with the latest theoretical calculation,[27] where the hole effective mass along *a*-direction is more than 10 times larger than that of *b*-direction. The steep variation on the resistivity ratio below 25 K needs further experimental studies in the future as stated above. This large anisotropy in resistivities along *a*- and *b*-directions may be the origin of the difference in resistivities of the thick Nb_2SiTe_4 single crystal as shown in Fig. 2(a). We speculate that the electrode arrangement in sample 2 is proximately towards the *a*-direction, and hence the obtained resistivity at 3 K is 10 times larger than that of sample 1.

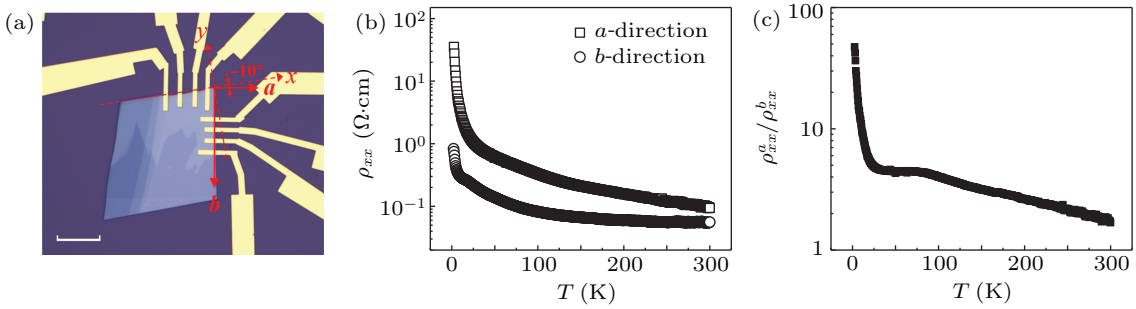


Fig. 5. Four-terminal resistivity measurement on a thin flake Nb_2SiTe_4 sample in the basal plane. (a) A device photo with a four-terminal electrode configuration. Scale bar: 20 μm. (b) Temperature dependence of resistivities along both *a*-direction (square) and *b*-direction (circle), respectively. (c) Temperature dependence of resistivity ratio of ρ^a_{xx}/ρ^b_{xx}.

4. Conclusion

To sum up, the electrical transport properties of layered Nb_2SiTe_4 are investigated and analyzed. It shows interesting semiconducting behaviors with large transport anisotropy in a wide temperature range. At temperature higher than 45 K, a hole carrier behavior is revealed with maximum carrier mobility 213 $cm^2 \cdot V^{-1} \cdot s^{-1}$ at 100 K, far higher than other reported experimental result and theoretical prediction. The carrier concentration is exponentially increased with temperature with a carrier active energy of 31.3 meV. Using the polarized Raman spectra, the crystallographic orientation of a thin flake Nb_2SiTe_4 is determined. Therefore, we can directly measure the resistivities ratio along the crystallographic *a*- and *b*-direction. The ratio is rapidly increased with temperature decreasing and reaches up to about 47.3 at 2.5 K. All of these are helpful to understand the interesting property of Nb_2SiTe_4 and provide valuable information for constructing Nb_2SiTe_4 based devices.

References

[1] Wu S F, Fatemi V, Gibson Q D, Watanabe K, Taniguchi T, Cava R J and Jarillo-Herrero P 2018 *Science* **359** 76
[2] Deng Y J, Yu Y J, Song Y C, Zhang J Z, Wang N Z, Sun Z Y, Yi Y F, Wu Y Z, Wu S W, Zhu J Y, Wang J, Chen X H and Zhang Y B 2018 *Nature* **563** 94
[3] Li J H, Yang L, Su S Q, Wang Z, Gu B L, Zhang S C, He K, Duan W H and Xu Y 2019 *Sci. Adv.* **5** eaaw5685
[4] Qiao J S, Kong X H, Hu Z X, Yang F and Wei J 2014 *Nat. Commun.* **5** 4475
[5] Ohtomo A and Hwang H Y 2004 *Nature* **427** 423
[6] Wu C C, Shang N Z, Zhao Z X, Zhang Z H, Liang J, Liu C, Zuo Y G, Ding M C, Wang J H, Hong H, Xiong J and Liu K H 2021 *Chin. Phys. B* **30** 027803
[7] Fan P, Qian G J, Wang D F, Li E, Wang Q, Chen H, Lin X and Gao H J 2021 *Chin. Phys. B* **30** 018105
[8] Fuhrer M S, Kim B M, Dürkop T and Brintlinger T 2002 *Nano Lett.* **2** 755
[9] Bao W Z, Cai X H, Kim D, Sridhara K and Fuhrer M S 2013 *Appl. Phys. Lett.* **102** 042104
[10] Buron J D, Pizzocchero F, Jepsen P U, Petersen D H, Caridad J M, Jessen B S, Booth T J and Bøggild P 2015 *Sci. Rep.* **5** 12305
[11] Shishir R S and Ferry D K 2009 *J. Phys.: Condens. Matter* **21** 232204
[12] Liu B B, Ma P J, Yu W J, Xu Y D and Gao L 2019 *Chin. Phys. Lett.* **36** 064202
[13] Tao R, Li L, Zhu L J, Yan Y D, Guo L H, Fan X D and Zeng C G 2020 *Chin. Phys. Lett.* **37** 077301
[14] Ruan Z L, Hao Z L, Zhang H, Sun S J, Zhang Y, Xiong W, Wang X Y, Lu J C and Cai J M 2021 *Chin. Phys. Lett.* **38** 027201
[15] Wu B L, Wei Q, Zhang Z Q and Jiang H 2021 *Chin. Phys. B* **30** 030504
[16] Zurrón Ó, Picón A and Plaja L 2018 *New J. Phys.* **20** 053033
[17] Gong C, Zhang H J, Wang W H, Colombo L, Wallace R M and Cho K 2013 *Appl. Phys. Lett.* **103** 053513
[18] Wu W, De D, Chang S C, Wang Y N, Peng H B, Bao J M and Pei S S 2013 *Appl. Phys. Lett.* **102** 142106
[19] Kim S, Konar A, Hwang W S, Lee J H, Lee J, Yang J, Jung C, Kim H, Yoo J B, Choi J Y, Jin Y W, Lee S Y, Jena D, Choi W and Kim K 2012 *Nat. Commun.* **3** 1011
[20] Jariwala D, Sangwan V K, Late D J, Johns J E, Dravid V P, Marks T J, Lauhon L J and Hersam M C 2013 *Appl. Phys. Lett.* **102** 173107
[21] Deng Y J, Yu Y J, Shi M Z, Guo Z X, Xu Z H, Wang J, Chen X H and Zhang Y B 2020 *Science* **367** 895
[22] Zhang S, Wang R, Wang X P, Wei B Y, Chen B, Wang H Q, Shi G, Wang F, Jia B, Ouyang Y P, Xie F J, Fei F C, Zhang M H, Wang X F, Wu D, Wan X G, Song F Q, Zhang H J and Wang B G 2019 *Nano Lett.* **20** 709
[23] Fu H X, Liu C X and Yan B H 2020 *Sci. Adv.* **6** eaaz0948
[24] Zhao M X, Xia W, Wang Y, Luo M, Tian Z, Guo Y F, Hu W D and Xue J M 2019 *ACS Nano* **13** 10705
[25] Monconduit L, Evain M, Brec R, Rouxel J and Canadell E 1993 *Comptes rendus de l'Acadéie des sciences serie II* **316** 25
[26] Zhang T, Ma Y D, Xu X L, Lei C G, Huang B B and Dai Y 2019 *J. Phys. Chem. Lett.* **11** 497
[27] Fang W Y, Li P A, Yuan J H, Xue K H and Wang J F 2020 *J. Electron. Mater.* **49** 959
[28] Hbivnák E 1960 *Czech. J. Phys. B* **10** 633
[29] Zhou K Y, Deng J, Guo L W and Guo J G 2020 *Chin. Phys. Lett.* **37** 097402
[30] Giannozzi P, Baroni S, Bonini N, *et al.* 2009 *J. Phys.: Condens. Matter* **21** 395502
[31] Schlipf M and Gygi F 2015 *Comput. Phys. Commun.* **196** 36
[32] Gong W T, Li L, Gong P L, Zhou Y L, Zhang Z T, Zhou W C, Wang W K, Liu Z R and Tang D S 2019 *Appl. Phys. Lett.* **114** 172104
[33] See https://www.cryst.ehu.es/rep/sam.html for "IR Raman and Hyper-Raman Modes" (last accessed January 2021)
[34] Liu Y N, Gu Q Q, Peng Y, Qi S M, Zhang N, Zhang Y N, Ma X M, Zhu R, Tong L M, Feng J, Liu Z and Chen J H 2018 *Adv. Mater.* **30** 1706402